Strathprints Institutional Repository

Droplet dynamics in confinement

N. Ioannou[a], H. Liu[b], Y.H. Zhang[a,*]

[a] *James Weir Fluids Laboratory, Department of Mechanical & Aerospace Engineering, University of Strathclyde, Glasgow G1 1XJ, UK*
[b] *School of Energy and Power Engineering, Xi'an Jiaotong University, Xi'an 710049, China*

A B S T R A C T

This study is to understand confinement effect on the dynamical behaviour of a droplet immersed in an immiscible liquid subjected to a simple shear flow. The lattice Boltzmann method, which uses a forcing term and a recolouring algorithm to realize the interfacial tension effect and phase separation respectively, is adopted to systematically study droplet deformation and breakup in confined conditions. The effects of capillary number, viscosity ratio of the droplet to the carrier liquid, and confinement ratio are studied. The simulation results are compared against the theoretical predictions, experimental and numerical data available in literature. We find that increasing confinement ratio will enhance deformation, and the maximum deformation occurs at the viscosity ratio of unity. The droplet is found to orient more towards the flow direction with increasing viscosity ratio or confinement ratio. Also, it is noticed that the wall effect becomes more significant for the confinement ratios larger than 0.4. Finally, the critical capillary number, above which the droplet breakup occurs, is found to be mildly affected by the confinement for the viscosity ratio of unity. Upon increasing the confinement ratio, the critical capillary number increases for the viscosity ratios less than unity, but decreases for the viscosity ratios more than unity.

© 2016 The Authors. Published by Elsevier B.V. This is an open access article under the CC BY license (http://creativecommons.org/licenses/by/4.0/).

1. Introduction

Emulsions consist of immiscible fluids commonly found in production processes in food, chemical, and pharmaceutical industries. Since the droplet size and shape determine important emulsion properties such as stability, rheology, and particle morphology, it is important to understand the mechanism of droplet deformation and breakup during emulsification. In addition, the study of droplet deformation and breakup can provide valuable insights into immiscible fluid displacement in porous media, which plays an important role in enhanced oil recovery, geologic CO_2 sequestration, and remediation of nonaqueous-phase liquids. In recent years, the droplet deformation and breakup have received more attention because of the growing interest in microfluidic technologies, where droplets are circulated in channels and their size is often comparable with or even smaller than channel dimension. A significant number of theoretical, experimental and numerical studies have been reported regarding droplet deformation and breakup in a shear flow since the pioneering work of Taylor [1]. The main feature of shear flow is its relative simplicity, while it contains rich physics [2].

As sketched in Fig. 1, a spherical droplet with radius R is initially placed halfway between two parallel plates that are separated by a distance H. Shear flow is introduced to this system by the movement of the plates with equal but opposite velocities U, and the resulting shear rate is $\dot{\gamma} = 2U/H$. The droplet and the carrier fluid are assumed to have equal densities ρ, a constant interfacial tension σ, and their dynamic viscosities are μ_d and μ_m. In the simple shear flow, two most important forces exerting on the droplet are: the viscous forces ($\mu_m \dot{\gamma} R^2$), leading the droplet to deform and turn towards the flow direction, and the capillary forces (σR), resisting the droplet deformation and retaining the spherical shape of the droplet. Consequently, the droplet undergoes an elongation in the direction of the L-axis, and a compression in the direction of the B-axis (see the right panel of Fig. 1). The capillary number, which is defined as $Ca = \dot{\gamma} R \mu_m / \sigma$, is used to measure the relative magnitude of viscous and capillary forces. The inertial force can also influence the dynamical behaviour of the droplet, and its importance is described by the Reynolds number, defined as the ratio of inertial to viscous forces i.e. $Re = \rho \dot{\gamma} R^2 / \mu_m$. In addition to the capillary and Reynolds numbers, the viscosity ratio ($\lambda = \mu_d / \mu_m$) and the proximity of droplet to the walls are found to affect strongly the deformation and breakup of the droplet. The proximity is evaluated by the confinement ratio, defined as $2R/H$. Under consideration of low capillary number and confinement ratio, the droplet will eventually become ellipsoidal in the Stokes flow regime ($Re < 1$). The

* Corresponding author.
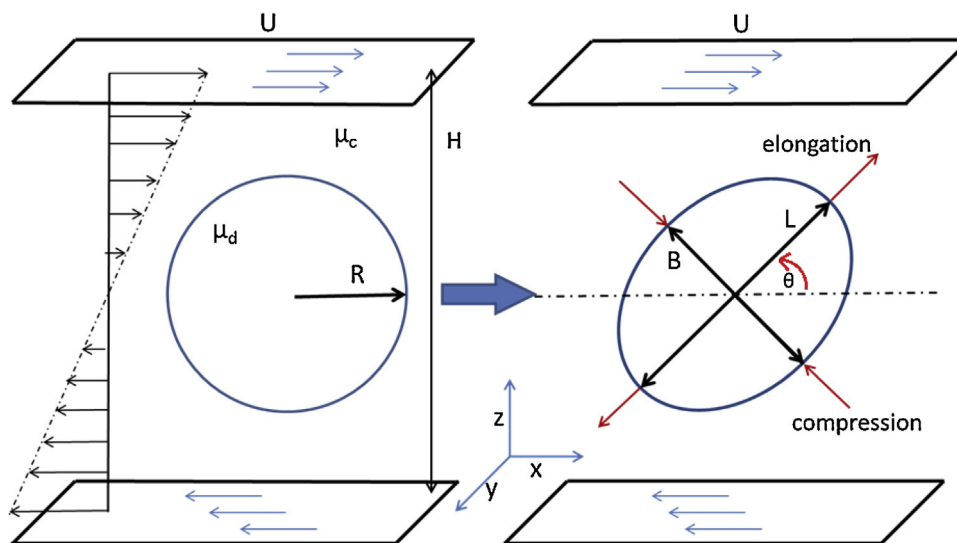   *E-mail address:* yonghao.zhang@strath.ac.uk (Y.H. Zhang).

Fig. 1. Schematic illustration of droplet deformation in a simple shear flow.

deformation parameter D can be defined by the lengths of the major (L) and minor (B) axes of the deformed droplet, i.e.

$$D = \frac{L - B}{L + B}. \tag{1}$$

With increasing Ca, the droplet can reach a steady state but deviate from the ellipsoidal shape. This causes difficulty in obtaining the correct values of deformation parameter and orientation angle (θ), which is defined as the angle between the droplet major axis and the horizontal plane. As the capillary number is further increased above the critical value, the capillary forces can no longer retain the shape of droplet; the dominant viscous forces lead the droplet to form a long thin neck and finally break up into two or more fragments. The critical capillary number (Ca_{cr}), above which the droplet breakup will occur, is influenced by both the viscosity and confinement ratios [3].

The interest in droplet deformation dates back to the work of Taylor (1934) [1], who derived a theoretical expression to describe small deformations in the bulk shear flow in terms of the viscosity ratio and the capillary number:

$$D_T = \frac{19\lambda + 16}{16\lambda + 16} Ca. \tag{2}$$

This expression has been demonstrated to predict experimental results well in a variety of cases, where the value of confinement ratio was around 0.2. However, the influence of wall confinement is not taken into account in Eq. (2). It was reported that the presence of walls has a negligible contribution to the droplet deformation for the confinement ratio $2R/H \leq 0.4$ [4,5]. When the confinement ratio is higher than 0.4, the deformation cannot be predicted accurately by Eq. (2). Moreover, Eq. (2) is not able to describe the droplet deformation for very large viscosity ratios [1,6]. More discussion about this equation can be found in these review papers [7–10]. Taylor derived his model using small deformation perturbation procedure to the first order, with Ca as the expansion parameter, so he obtained a constant orientation angle of $45°$. The perturbation procedure was later to be extended to the second order in Ca to yield an expression for the orientation angle [11–14]: $\theta = (\pi/4) - ((16 + 19\lambda)(3 + 2\lambda)/80(1 + \lambda))Ca$ [15]. The orientation angle was also formulated differently in the phenomenological models of Maffettone and Minale [16] and Minale [17].

To address the wall confinement effect on droplet behaviour, Shapira and Haber [18] solved the Stokes flows around a droplet using the method of reflection, which takes into account the relative position of the droplet to the wall. The resulting SH model combines the Taylor deformation and an additional term accounting for the influence of walls on the deformation:

$$D_{SH} = D_T \left[1 + C_S \frac{1 + 2.5\lambda}{1 + \lambda} \left(\frac{R}{H} \right)^3 \right], \tag{3}$$

where C_S is referred to as a shape parameter and its value depends on the relative position of the droplet to the walls. For a droplet positioned halfway between the two walls C_S is taken as 5.6996.

To predict the droplet deformation under transient conditions, Maffettone and Minale [16] proposed a phenomenological model, i.e. MM model, in which the droplet shape is assumed to remain ellipsoidal. A second order tensor $\mathcal{S}$, whose eigenvalues reflect the squares of the semi-axes of an ellipsoid, is used to describe the droplet shape. Based on this assumption, they derived an evolution equation for the tensor $\mathcal{S}$, which consists of a co-rotational derivative, the contributions of the viscous stress and the capillary force. The values of the semi-axes for several typical flows were predicted, including the simple shear flow, the uniaxial extensional flow and the planar hyperbolic flow. In particular, for the simple shear flow, the deformation parameter in a steady state is calculated as

$$D_{MM} = \frac{\sqrt{m_1^2 + Ca^2} - \sqrt{m_1^2 + (1 - m_2^2)Ca^2}}{m_2 Ca}, \tag{4}$$

where

$$m_1 = \frac{40(\lambda + 1)}{(2\lambda + 3)(19\lambda + 16)}, \tag{5}$$

and

$$m_2 = \frac{5}{2\lambda + 3} + \frac{3Ca^2}{2 + 6Ca^2}. \tag{6}$$

The droplet deformation was also investigated experimentally by Sibillo et al. [19] for the viscosity ratio of unity. Three different capillary numbers, i.e. 0.1, 0.2, and 0.3, were studied for the confinement ratios ranging from 0.14 to 1.0. For the same capillary number, the droplet could obtain a more elongated shape for larger confinement ratios. Also, the droplet shape deviates from ellipsoid at very high confinement ratios, i.e., $2R/H \geq 0.8$. A similar study, for a range of viscosity ratios, was performed by Vananroye et al. [6]. The difference in the droplet deformation is not significant for different viscosity ratios at low confinement ratios. However, this difference grows considerably at large confinement ratios, and is more

significant at large capillary numbers. In an attempt to match the experimental results regarding large deformation at large capillary numbers (e.g., $Ca = 0.3$) with an analytical expression, two models were proposed. One is the orientation angle scaled SH model. However, it suffers from the difficulty of estimating the orientation angle at high confinement ratios [7]. The other is a combination of the aforementioned two models (i.e., SH and MM). Specifically, the term D_T in the SH model is replaced by D_{MM} in the MM model, leading to a new model, called as the MMSH model:

$$D_{MMSH} = D_{MM} \left[1 + C_S \frac{1 + 2.5\lambda}{1 + \lambda} \left(\frac{R}{H} \right)^3 \right]. \tag{7}$$

Since the MMSH model does not need to estimate the droplet orientation angle and its predictions agree well with the experimental data [6], it will be used in Section 3 for validation of our numerical results. In addition, Minale [17] refined the phenomenological MM model, by forcing the model to recover the analytical limits of the SH model for moderate confinement ratios, i.e. $2R/H \leq 0.5$. For large confinement ratios, the experimental data from Sibillo et al. [19] and Vananroye et al. [6], were used to re-evaluate the coefficients m_1 and m_2 in the MM model.

Complementing theoretical and experimental studies, numerical simulations have been extensively used to investigate the droplet deformation and breakup in a simple shear flow [3,4,20–24]. Among these works, Janssen and his co-workers [3,23,24] used the boundary integral method (BIM) to study the effect of viscosity and confinement ratios on droplet deformation and the critical capillary number. It was found that the simulated shape of the droplet and the critical capillary number are both in excellent agreement with the experimental results. However, the BIM is usually for the solution of Stokes flow, in which the fluid inertia is totally neglected. Also, it suffers from the difficulties of accessing the low viscosity ratio regime [3], and of dealing with topological changes such as breakup and coalescence of the interfaces [7,25,26]. These disadvantages can be overcome by the lattice Boltzmann method (LBM), which tracks evolution of the distribution function of an assembly of molecules and is built upon microscopic models and mesoscopic kinetic equations. The LBM can capture multiphase interface and describe interfacial dynamics such as phase segregation and interfacial tension through the incorporation of intermolecular interactions. A number of multiphase and multicomponent models have been proposed, which can be divided into four main types: colour gradient model [27], free-energy model [28], interparticle-potential model [29], and mean-field theory model [30]. Although the droplet dynamics in a shear flow was successfully simulated by the former three models or their variants [31–36], none of them has systematically examined the impact of viscosity and confinement ratios on the droplet deformation and breakup, which is the focus of this work. In particular, the colour gradient LBM is used here because of its advantages such as low spurious currents, high numerical accuracy and strict mass conservation for each fluid which have been demonstrated in our recent works [37,38].

2. Numerical method

We consider isothermal motion of two immiscible fluids and adopt a continuum surface force (CSF) model [39] to describe the system. The CSF formulation allows us to consider the two phases as a single fluid with space-dependent properties and replaces the jump condition at the interface with an additional force that acts only in the interface region. Unlike a two-fluid formulation, it does not need to solve a moving boundary problem, which is computationally expensive and extremely difficult to implement especially when large topological changes occur around the

interface. In the CSF formulation, the flow of two immiscible fluids is governed by a single set of Navier–Stokes equations (NSEs):

$$\nabla \cdot \vec{u} = 0, \tag{8}$$

$$\frac{\partial(\rho\vec{u})}{\partial t} + \nabla \cdot \left(\rho \vec{u}\vec{u} \right) = -\nabla p + \nabla \cdot [\mu(\nabla\vec{u} + \nabla\vec{u}^T)] + \vec{F}_s, \tag{9}$$

where t is the time, $\vec{u}$ is the fluid velocity, ρ is the total density, p is the pressure, and μ is the dynamic viscosity. The last term in Eq. (9) represents the interfacial tension force acting at the interface between the two fluids and is defined as

$$\vec{F}_s = \sigma\kappa\vec{n}\delta_\Gamma, \tag{10}$$

where σ is the interfacial tension; κ, the local interface curvature; $\vec{n}$, the unit normal to the interface; and δ_Γ, the Dirac delta function used to localize the force explicitly at the interface, which should satisfy

$$\int_{-\infty}^{\infty} \delta_\Gamma dz = 1, \tag{11}$$

in order to recover properly the stress jump condition in the sharp-interface limit. Here z is the spatial location normal to the interface.

Although Eqs. (8) and (9) allow computing the velocity field, an advection equation has to be additionally solved to capture the evolution of interface in traditional multiphase solvers, e.g., the volume-of-fluid (VOF) and level-set methods, where the sophisticated interface reconstruction algorithm or unphysical re-initialization process is often required. In order to avoid these issues, we use the lattice Boltzmann colour gradient model, first proposed by Gunstensen et al. [27] and later improved by Halliday and his coworkers [40], to simulate the dynamical behaviour of a droplet subjected to a simple shear flow. The colour gradient model possesses many advantages in simulating immiscible two-phase flows, including the ability of capturing interface automatically, low spurious velocities, high numerical accuracy and strict mass conservation for each fluid. In this model, two sets of distribution functions f_i^R and f_i^B are introduced to represent the "red" and "blue" fluids. The total distribution function is defined by $f_i = f_i^R + f_i^B$, which undergoes a Bhatnagar–Gross–Krook (BGK) collision step as

$$f_i^\dagger(\vec{x}, t) = f_i(\vec{x}, t) - \frac{1}{\tau}(f_i(\vec{x}, t) - f_i^{eq}(\vec{x}, t)) + \Phi_i, \tag{12}$$

where $f_i(\vec{x}, t)$ is the total distribution function in the ith velocity direction at the position $\vec{x}$ and time t, f_i^{eq} is the equilibrium distribution function of f_i, $f_i^\dagger$ is the post-collision distribution function, τ is the dimensionless relaxation time, and Φ_i is the forcing term.

The equilibrium distribution function is obtained by a second-order Taylor expansion of Maxwell–Boltzmann distribution with respect to the local velocity $\vec{u}$:

$$f_i^{eq} = \rho w_i \left[1 + \frac{\vec{e}_i \cdot \vec{u}}{c_s^2} + \frac{(\vec{e}_i \cdot \vec{u})^2}{2c_s^4} - \frac{\vec{u}^2}{2c_s^2} \right], \tag{13}$$

where ρ is calculated by $\rho = \rho_R + \rho_B$ with the subscripts 'R' and 'B' referring to the red and blue fluids respectively, c_s is the speed of sound, $\vec{e}_i$ is the lattice velocity in the ith direction, and w_i is the weight factor. For the three-dimensional 19-velocity (D3Q19) model, the lattice velocity $\vec{e}_i$ and the weight factors are given by

$$\vec{e}_i = \begin{cases} (0, 0, 0)c, & i = 0; \\ (\pm 1, 0, 0)c, (0, \pm 1, 0)c, (0, 0, \pm 1)c, & i = 1, 2, \ldots, 6; \\ (\pm 1, \pm 1, 0)c, (0, \pm 1, \pm 1)c, (\pm 1, 0, \pm 1)c, & i = 7, 8, \ldots, 18, \end{cases}$$
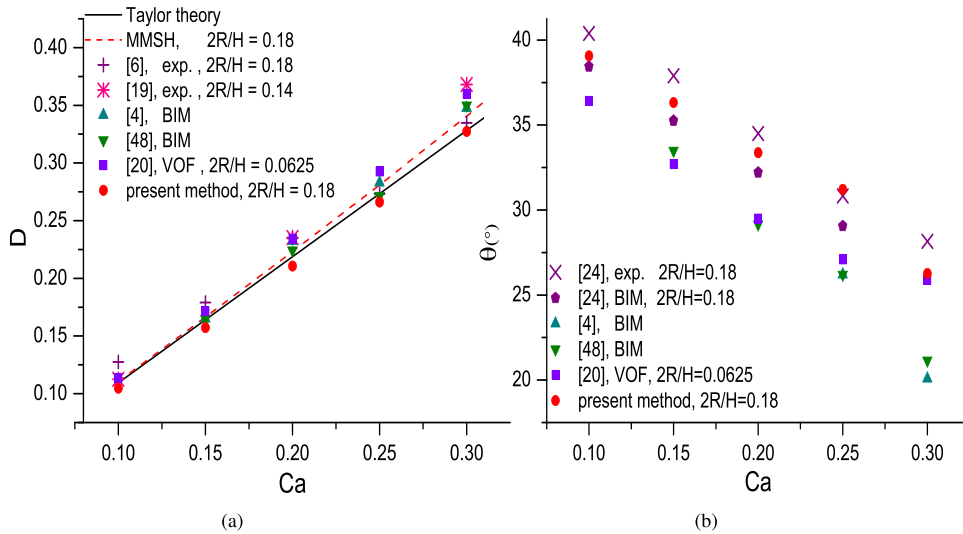
$$\tag{14}$$

Fig. 2. The deformation parameter (a), and the orientation angle (b) as a function of the capillary number for $\lambda = 1$.

$$w_i = \begin{cases} 1/3, & i = 0; \\ 1/18, & i = 1, 2, \ldots, 6; \\ 1/36, & i = 7, 8, \ldots, 18, \end{cases} \quad (15)$$

and the speed of sound $c_s = c/\sqrt{3} = \delta_x/\sqrt{3}\delta_t$ with δ_x and δ_t being the lattice length and time step, respectively.

The spatial distribution of the two fluids is described using a colour function (or phase-field function), which is defined as

$$\rho^N(\vec{x}, t) = \frac{\rho_R(\vec{x}, t) - \rho_B(\vec{x}, t)}{\rho_R(\vec{x}, t) + \rho_B(\vec{x}, t)}, \quad -1 \leq \rho^N \leq 1. \quad (16)$$

By defining $\vec{n} = -\nabla\rho^N/|\nabla\rho^N|$ and $\delta_\Gamma = |\nabla\rho^N|/2$, Eq. (10) can be further written as

$$\vec{F}_s = -\frac{1}{2}\sigma\kappa\nabla\rho^N, \quad (17)$$

where the local interface curvature κ is related to the unit normal to the interface by

$$\kappa = -\left[(\mathbf{I} - \vec{n} \otimes \vec{n}) \cdot \nabla\right] \cdot \vec{n} = -\nabla \cdot \vec{n}, \quad (18)$$
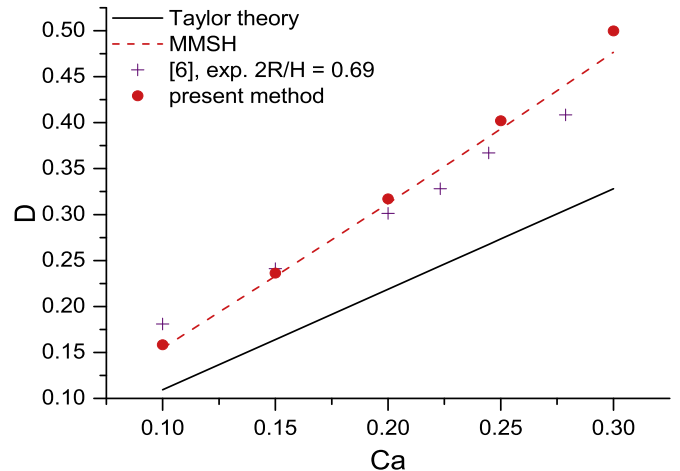
Fig. 3. Deformation parameter as a function of the capillary number for $\lambda = 1$ and $2R/H = 0.69$.
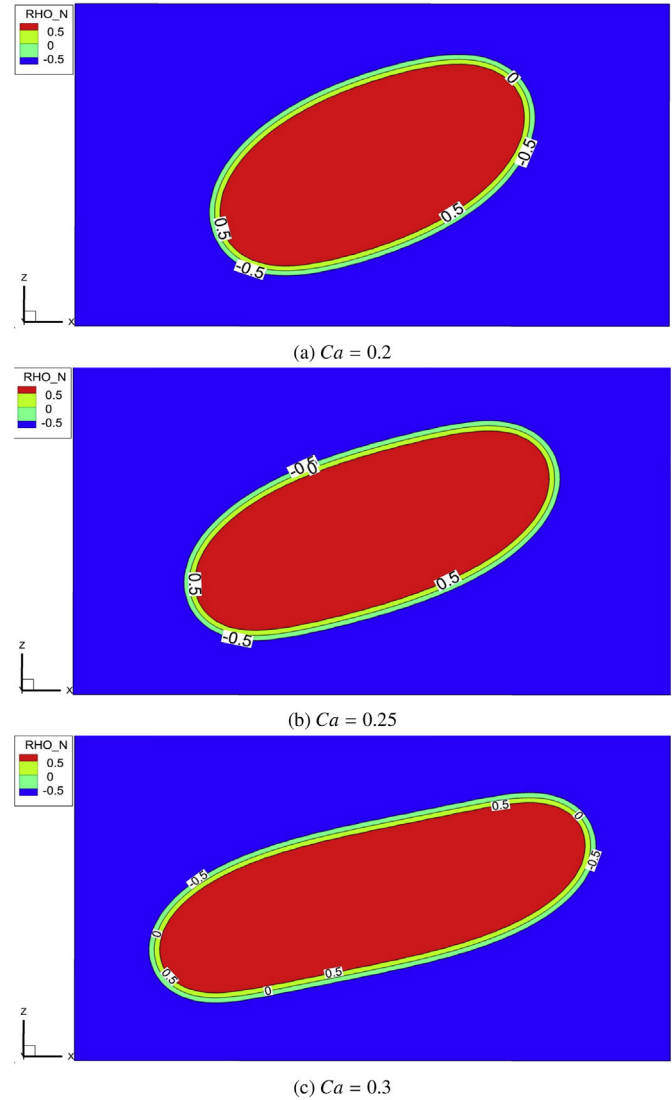

(a) $Ca = 0.2$

(b) $Ca = 0.25$

(c) $Ca = 0.3$

Fig. 4. Final shape of the deformed droplet in the middle x–z plane for $\lambda = 1$ and $2R/H = 0.69$ at different capillary numbers: (a) $Ca = 0.2$, (b) $Ca = 0.25$, and (c) $Ca = 0.3$.

and **I** is the second-order identity tensor. With the interfacial tension force given by Eq. (17), the forcing term Φ_i that is applied to realize the interfacial tension effect, reads as [41]

$$\Phi_i = \left(1 - \frac{1}{2\tau}\right) w_i \left(\frac{\vec{e}_i - \vec{u}}{c_s^2} + \frac{\vec{e}_i \cdot \vec{u}}{c_s^4}\vec{e}_i\right) \cdot \vec{F}_s \delta_t. \tag{19}$$

According to Guo et al. [42], the local fluid velocity should be defined to incorporate the spatially varying interfacial tension force, i.e.,

$$\rho \vec{u}(\vec{x}, t) = \sum_i f_i(\vec{x}, t)\vec{e}_i + \frac{1}{2}\vec{F}_s(\vec{x}, t)\delta_t. \tag{20}$$

Using the Chapman–Enskog multiscale expansion, Eq. (12) can reduce to the NSEs in the low frequency, long wavelength limit with the pressure and the fluid viscosity defined by

$$p = \rho c_s^2, \tag{21}$$

$$\mu = \rho c_s^2 \left(\tau - \frac{1}{2}\right)\delta_t. \tag{22}$$

To allow for unequal viscosities of the two fluids, we determine the viscosity of the fluid mixture by a harmonic mean, i.e.

$$\frac{1}{\mu\left(\rho^N\right)} = \frac{1 + \rho^N}{2\mu_R} + \frac{1 - \rho^N}{2\mu_B}, \tag{23}$$

where μ_k ($k = R$ or B) is the dynamic viscosity of fluid k. It has been shown that the choice of Eq. (23) can ensure a constant viscosity stress across the interface, which provides higher accuracy than other choices [43].

The partial derivatives required for the curvature and normal vector calculations are obtained using the 19-point compact
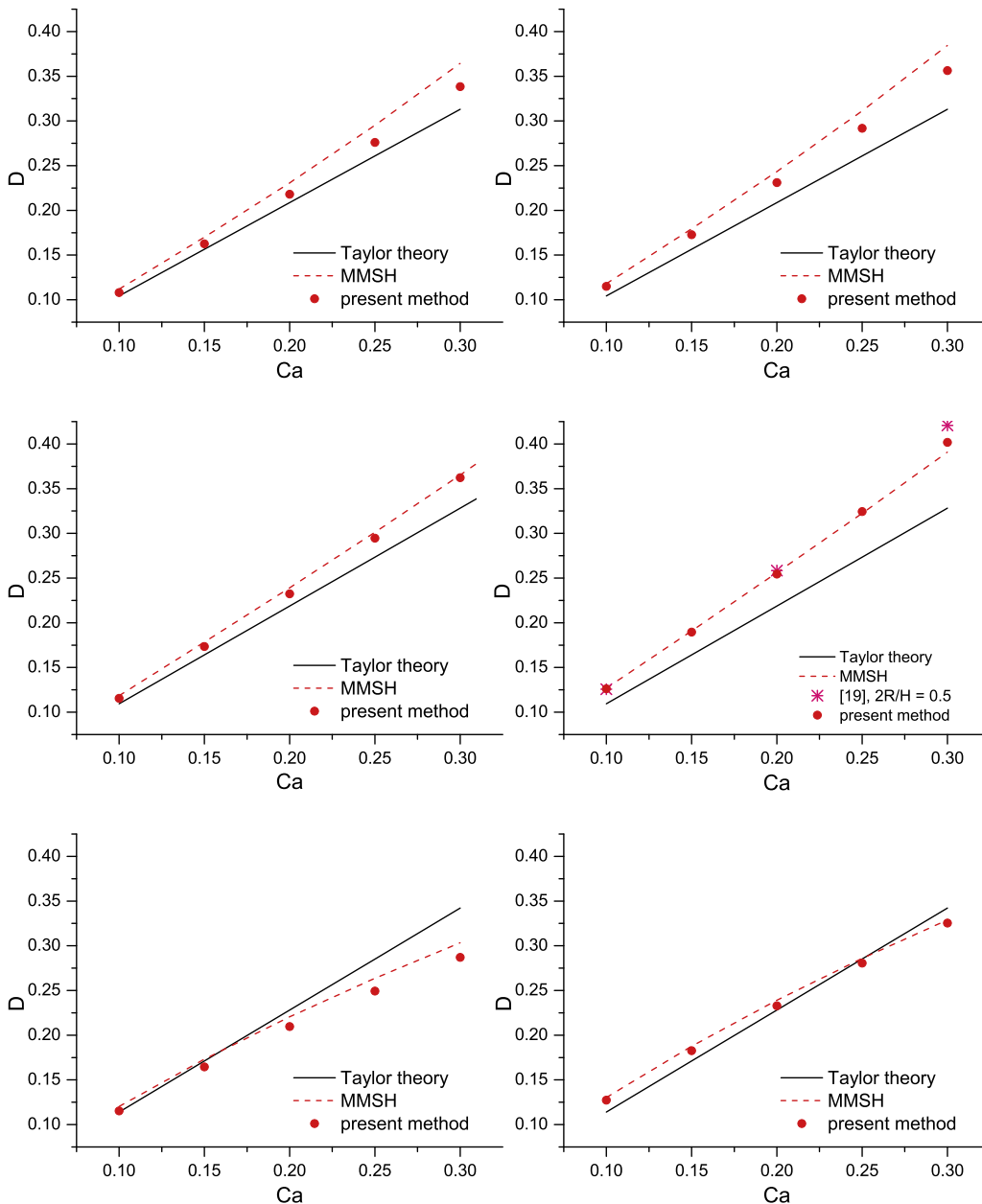

Fig. 5. Deformation parameter as a function of the capillary number for various parameters, each column has the same confinement ratio (left: $2R/H = 0.4$, right: $2R/H = 0.5$), and each row has the same viscosity ratio (top: $\lambda = 0.3$, middle: $\lambda = 1$, bottom: $\lambda = 3$).

finite-difference stencil [44]. For example, for a variable ψ, its partial derivatives can be calculated by

$$\frac{\partial \psi(\vec{x})}{\partial x_a} = \frac{1}{c_s^2} \sum_i w_i \psi(\vec{x} + \vec{e}_i \delta_t) e_{ia}. \qquad (24)$$

Although the forcing term generates an interfacial tension, it does not guarantee the immiscibility of both fluids. To promote phase segregation and maintain a reasonable interface, the segregation (recolouring) algorithm of Latva-Kokko and Rothman is used [45]. It can overcome the lattice pinning problem and creates a symmetric distribution of particles around the interface so that unphysical spurious currents can be effectively reduced. Following Latva-Kokko and Rothman, the post-segregation (recoloured) distribution functions of the red and blue fluids are

$$f_i^R(\vec{x}, t) = \frac{\rho_R}{\rho} f_i^\dagger(\vec{x}, t) + \beta \frac{\rho_R \rho_B}{\rho} w_i \cos(\varphi_i)|\vec{e}_i|,$$
$$f_i^B(\vec{x}, t) = \frac{\rho_B}{\rho} f_i^\dagger(\vec{x}, t) - \beta \frac{\rho_R \rho_B}{\rho} w_i \cos(\varphi_i)|\vec{e}_i|, \qquad (25)$$

where β is the segregation parameter and is set to be 0.7 for numerical stability and model accuracy [46]; φ_i is the angle between the colour gradient and the lattice vector $\vec{e}_i$, which is defined by

$$\cos(\varphi_i) = \frac{\vec{e}_i \cdot \nabla \rho^N}{|\vec{e}_i||\nabla \rho^N|}. \qquad (26)$$

After the recolouring step, the red and blue distribution functions propagate to the neighbouring lattice nodes, known as propagation or streaming step:

$$f_i^k(\vec{x} + \vec{e}_i \delta_t, t + \delta_t) = f_i^k(\vec{x}, t), \quad k = R \text{ or } B, \qquad (27)$$

and the resulting distribution functions are then used to calculate the densities of both fluids i.e. $\rho^k = \sum_i f_i^k$.

3. Results and discussion

In all the cases discussed below, a spherical droplet with the radius $R = 20$ lattices is initially placed in the centre of the computational domain, as illustrated in Fig. 1. The computational domain has a length of 71 lattices in the y-direction. The length in the x-direction is chosen as 101 in the study of droplet deformation, whereas in droplet break-up this length could be increased up to 401 in some cases in order to avoid the occurrence that the droplet touches itself via the periodic boundary conditions before the breakup occurs. In addition, the height of the computational

domain is varied in the range of $51 \leq H \leq 223$ to obtain different confinement ratios $2R/H$. Periodic boundary conditions are applied in the x- and y-directions, while the half-way bounce-back scheme is used on the top and bottom walls [47]:

$$f_i(\vec{x}, t + \delta_t) = f_{ops(i)}^\dagger(\vec{x}, t) + 6 w_i \rho \frac{\vec{e}_i \cdot \vec{u}_w}{c}, \qquad (28)$$

where $\vec{u}_w$ is the moving velocity of the solid wall with $\vec{u}_w = (U, 0, 0)$ for the top wall and $\vec{u}_w = (-U, 0, 0)$ for the bottom wall, and $ops(i)$ stands for the distribution function which has opposite direction to $\vec{e}_i$. For the sake of simplicity, both fluids are assumed to have equal densities. The Reynolds number is fixed at 0.1, which is small enough to characterise the flow as Stokes flow.

3.1. Droplet deformation

The numerical method is first tested by simulating the droplet deformation in a weakly confined shear flow. Simulations are conducted at $\lambda = 1$ and the confinement ratio $2R/H = 0.18$ for the capillary numbers ranging from 0.1 to 0.3. Fig. 2(a) plots the droplet deformation parameter as a function of the capillary number, in which our LBM results are compared with the previous experimental data [6,19], the numerical results obtained by the boundary integral method (BIM) [4,48] and the volume of fluid (VOF) method [20], as well as the predictions from Taylor theory and MMSH model. Note that the degree of confinement is not explicitly available for some of the data sources, in which the flow is considered to be unbounded. It can be seen from the comparison, the LBM results agree well with these experimental data, numerical results and model predictions; and good agreement among them suggests that the walls have a negligible influence on the droplet behaviour for the present confinement ratio, i.e. $2R/H = 0.18$, consistent with the previous numerical and experimental observations [4,8].

In addition to the deformation parameter, we also calculate the orientation angles of the deformed droplet (θ), defined as the angle between the longest axis of the droplet and the x-axis, at various capillary numbers, and compare them to those reported in Refs. [4,20,24,48] (see Fig. 2(b)). Clearly, there is fairly good agreement especially between our results and those obtained by the experiment and the BIM *at an exactly matched confinement ratio, i.e.* $2R/H = 0.18$.

Next, the simulations were conducted for a high confinement of 0.69, which is achieved by adjusting the height of computational domain whilst keeping other parameters the same as in Fig. 2. Fig. 3 shows the comparison between the simulated deformation
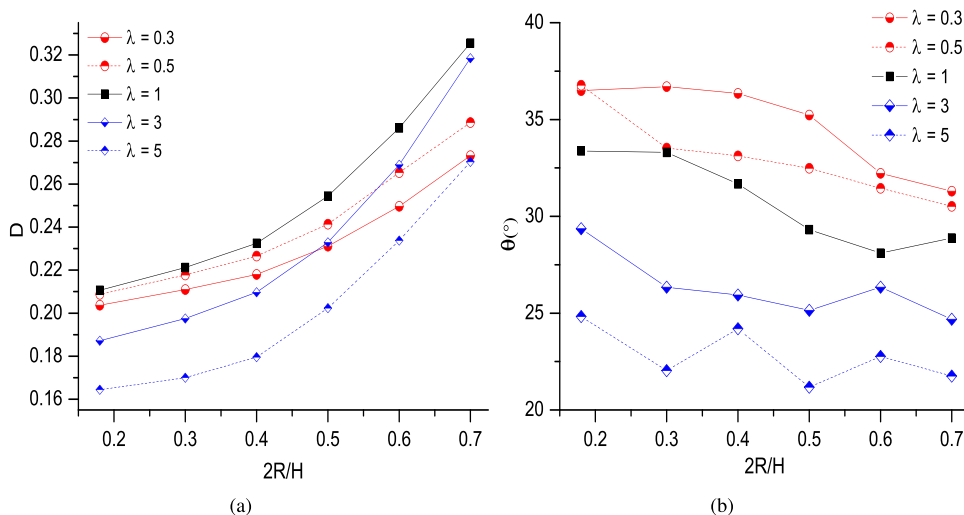

Fig. 6. Deformation parameter (a), and orientation angle (b) versus the confinement ratio for various viscosity ratios.
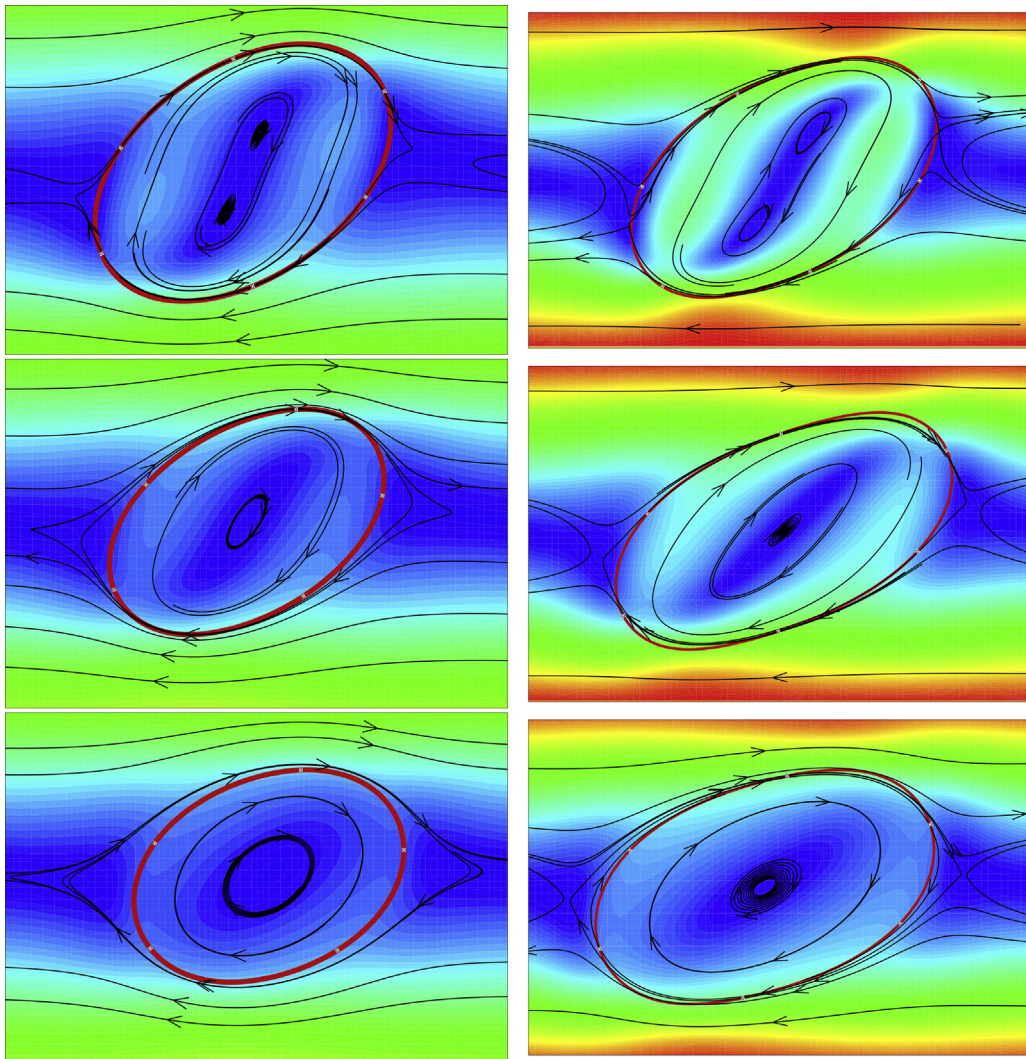
Fig. 7. Velocity vectors and streamlines around the droplet for $Ca = 0.2$: the columns are for the same confinement ratio (left: 0.4, right: 0.7); and the rows are for the same viscosity ratio (top: $\lambda = 0.3$, middle: $\lambda = 1$, bottom: $\lambda = 5$).

parameter and the Taylor theory, the MMSH model and the experimental results of Vananroye et al. [6]. Consistent with the previous findings, the MMSH model can provide experimentally-matched predictions of the droplet deformation, but the predictions from the Taylor theory are no longer valid for high confinement ratios. Also, our simulation results again match quite well with the predictions from the MMSH model and the experimental data, verifying that the present LBM can successfully predict deformation of a highly confined droplet. Fig. 4 shows the final shape of the deformed droplet in the middle x–z plane for $Ca = 0.2$, 0.25 and 0.3, in which the contours with $\rho^N = -0.5$, 0, and 0.5 are displayed. It is observed that the droplet deviates from the ellipsoidal shape to some extent at high capillary numbers, e.g. $Ca = 0.25$ and 0.3. Therefore, the confinement ratio and the capillary number are restricted to $2R/H \leq 0.7$ and $Ca \leq 0.3$, and both of them will not take large values at the same time in the rest of the simulations in order to ensure that the deformed droplet maintains an ellipsoidal shape.

Then, the effect of viscosity ratio on droplet deformation is studied at two moderate confinement ratios, 0.4 and 0.5. For each confinement ratio, three different viscosity ratios are considered, i.e. $\lambda = 0.3$, 1, and 3. The variation of deformation parameter with the capillary number is presented in Fig. 5. For the viscosity ratio of 0.3, our LBM results agree well with the MMSH model at low Ca, but gradually deviate from the MMSH model with increasing Ca.

Specifically, our LBM results lie between the Taylor theory and the MMSH model. The reason for the deviation remains an open question and needs further study. Note that similar observations were reported experimentally by Vananroye et al. [6]. For the viscosity ratio of unity, our LBM results agree quite well with the MMSH model, and the experimental data [19] where the data were only for

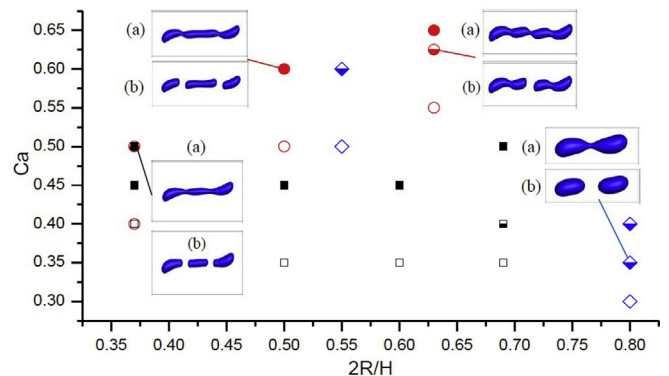

Fig. 8. Capillary numbers at which the droplet obtains a steady shape or experience break-up, for different viscosity ratios and confinements. The symbols are explained in the text. Inset: droplet shape before (a), and after (b) the breakup.

the confinement ratio of 0.5. For the viscosity ratio of 3, the obtained results of droplet deformation are a little lower than the predictions from the MMSH model for the confinement ratio of 0.4, whereas for the confinement ratio of 0.5 one can clearly observe excellent agreement between the simulations and the MMSH model. Moreover, our results deviate significantly from the Taylor theory for both $2R/H = 0.4$ and $2R/H = 0.5$. Thus, it can be concluded that the Taylor theory cannot describe droplet deformation in confinement with the confinement ratio as small as 0.4, which is somehow different from the previous finding i.e. the wall effects can be neglected when $2R/H \leq 0.4$ [4].

The effect of the confinement and viscosity ratios is further investigated at a fixed capillary number of 0.2. The confinement ratio ranges from 0.18 to 0.7. Fig. 6(a) shows the variation of the deformation parameter for $\lambda = 0.3$, 0.5, 1, 3, and 5. It is observed that the deformation increases with increasing viscosity ratio up to unity. Upon a further increase of the viscosity ratio, the deformation decreases. In addition, we observe that increasing confinement ratio leads to bigger deformation of the droplet for all the viscosity ratios. Interestingly, the droplet deformation does not present a linear correlation with the proximity of the walls. It increases almost linearly, with different rates, before and after $2R/H = 0.4$. Up to this value the deformation exhibits a slow increase, which becomes more rapid upon higher values, especially for the high viscous droplets. This can be explained together with the corresponding orientation angles. The variation of the corresponding

(a) $\dot{\gamma}t = 0$ (b) $\dot{\gamma}t = 4$

(c) $\dot{\gamma}t = 9$ (d) $\dot{\gamma}t = 17$

(e) $\dot{\gamma}t = 25$ (f) $\dot{\gamma}t = 34$

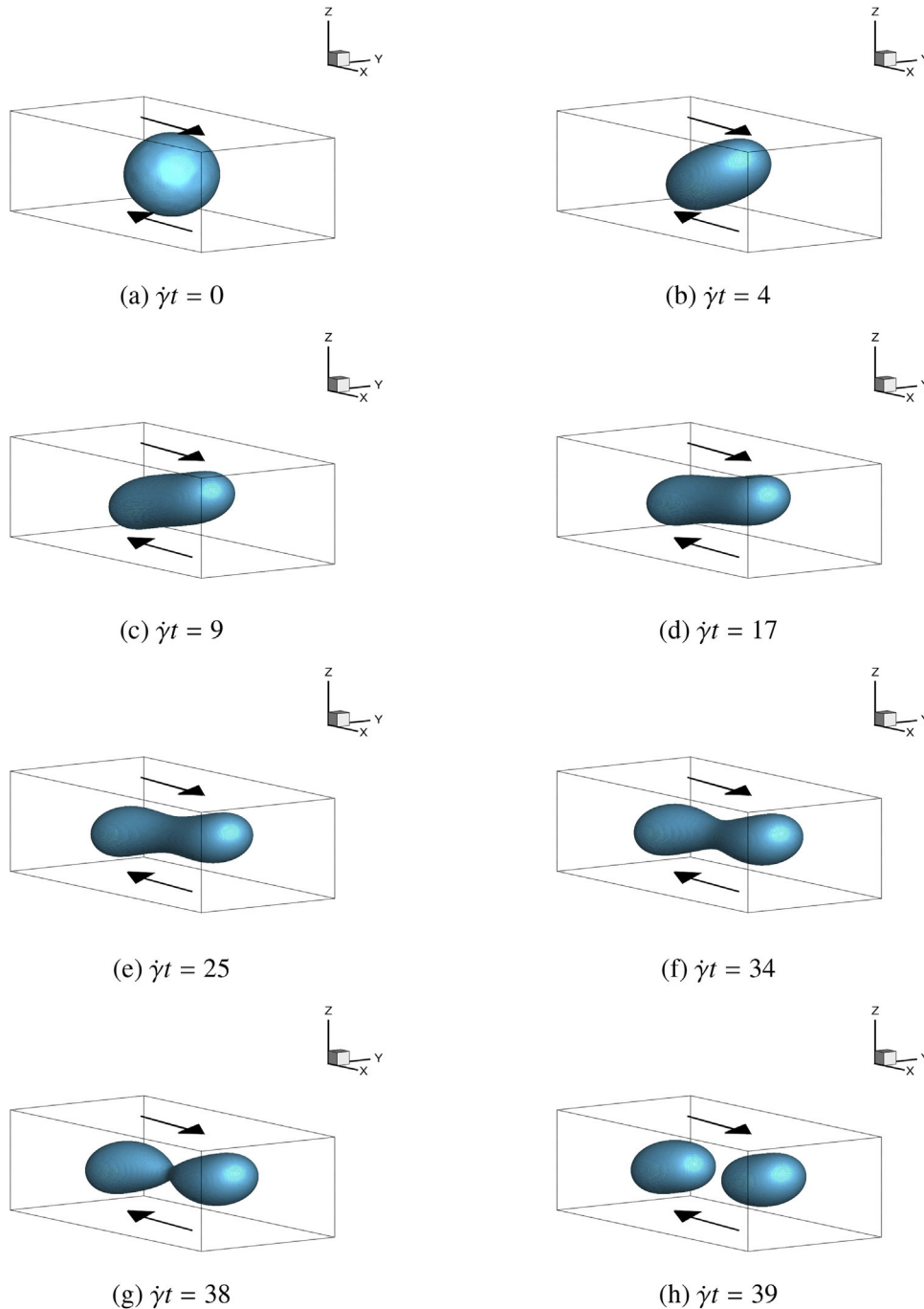(g) $\dot{\gamma}t = 38$ (h) $\dot{\gamma}t = 39$

Fig. 9. Transient droplet shape for $Ca = 0.35$, $\lambda = 5$ and $2R/H = 0.8$.

orientation angle (θ) with the confinement ratio is shown in Fig. 6(b). Increasing viscosity ratio causes the droplet to align more with the shear flow, thus resulting in a smaller orientation angle. For $\lambda \geq 1$, both the deformation parameter (see Fig. 6(a)) and the orientation angle (Fig. 6(b)) reveal more significant variations with the confinement ratio $2R/H \geq 0.4$. This suggests that the wall confinement has a stronger effect on droplet deformation for more viscous droplets. For $\lambda = 3, 5$, the orientation angles do not reduce further once $2R/H \geq 0.3$. Therefore, the carrier fluid has a narrower flow passage to pass the droplet which leads to built-up shear stress around the droplet. Consequently, the deformation rate increases more rapidly for $\lambda = 3, 5$ with increasing confinement.

In order to illustrate the effect of the viscosity ratio and the confinement ratio on the flowfield inside and around the droplet, Fig. 7

(a) $\dot{\gamma}t = 0$

(b) $\dot{\gamma}t = 4$

(c) $\dot{\gamma}t = 8$

(d) $\dot{\gamma}t = 12$

(e) $\dot{\gamma}t = 16$

(f) $\dot{\gamma}t = 20$

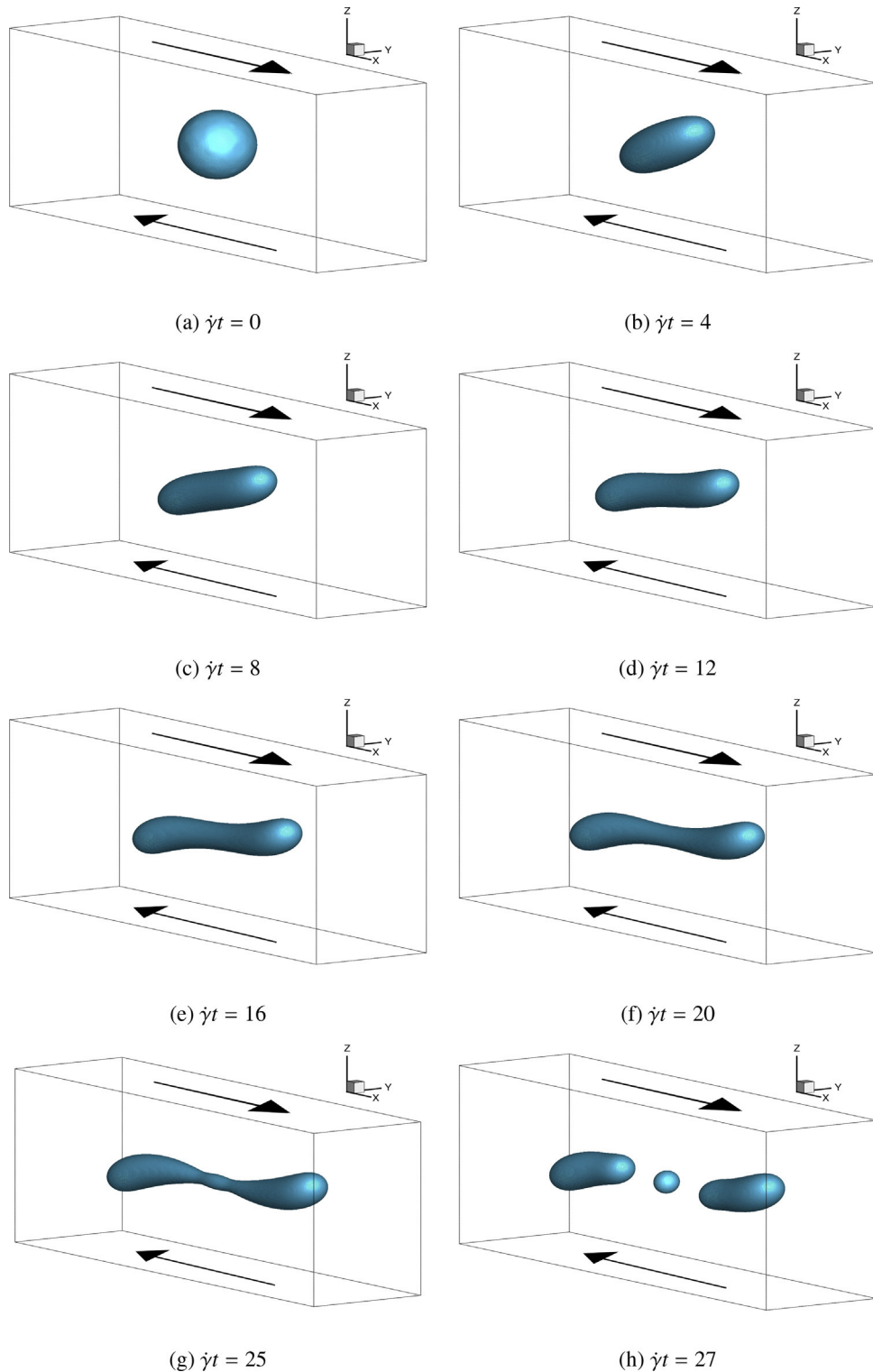(g) $\dot{\gamma}t = 25$

(h) $\dot{\gamma}t = 27$

Fig. 10. Transient droplet shape for $Ca = 0.45$, $\lambda = 1$ and $2R/H = 0.4$.

depicts the velocity contours and streamlines in the middle x–z plane for $2R/H = \{0.4, 0.7\}$ and $\lambda = \{0.3, 1, 5\}$ at $Ca = 0.2$. Note that we here limit our investigation to $2R/H = 0.4$ and 0.7 since the impact of wall becomes more evident with the confinement ratio larger than 0.4. In this figure, the thick solid lines represent the droplet interface where $\rho^N = 0$, while the black solid lines represent the streamlines, with arrows indicating the direction of the local flow. It is confirmed that the effect of the viscosity ratio and the confinement ratio are not only on the droplet shape and orientation angle, but also on the flowfield patterns inside and around the droplet. Increasing viscosity ratio leads to the streamline pattern inside the droplet varying from a double vortex to a single vortex structure. Interestingly, an analogous variation in the streamline pattern was observed in the previous numerical studies [20,21,34,35] when the Reynolds number is decreased from a relatively high value. In addition, as the viscosity ratio increases, the inclination angle of the internal vortices (streamlines) and the orientation angle of the droplet both decrease, and their difference also reduces. For two different confinement ratios, the streamline patterns are qualitatively similar but quantitatively different, e.g. the inclination of streamlines inside the droplet is smaller at the confinement ratio of 0.7, which corresponds to a larger deformation and smaller orientation angle of the droplet.

3.2. Droplet breakup

In this section, we investigate the critical capillary number of the droplet breakup at various viscosity and confinement ratios. The simulations are conducted for the confinement ratios ranging from 0.37 to 0.8 at three typical viscosity ratios, i.e. $\lambda = 0.3$, 1 and 5. Although the LBM has been used extensively to simulate the droplet breakup, e.g., Refs. [32–35], to the best of our knowledge, no studies to date have considered such a broad range of parameters. This is partially because of the unsolved issues of the existing models themselves, such as artificially enlarged interface thickness and case-dependent mobility in the phase-field-based model, high spurious currents, numerical instability in the interparticle-potential model.

Fig. 8 shows the effect of the confinement ratio on the droplet breakup at the viscosity ratios of 0.3, 1, and 5, which are represented by circles, squares, and diamonds, respectively. Empty symbols are used in the cases where no droplet breakup is observed. To distinguish different modes of breakup, we use half-filled symbols to denote the binary breakup, and full-filled symbols to denote the multiple breakup, where the droplet splits into three or more daughter droplets. In addition, the breakup is depicted at the moments before and after it occurs, for a number of cases. Following the aforementioned definition, the critical capillary number, Ca_{cr}, lies between the empty and filled symbols. The confinement ratio has different effects on the critical capillary number, depending on the viscosity ratio. For the low viscosity ratio, i.e. $\lambda = 0.3$, the critical capillary number is varied from $0.4 \leq Ca_{cr} \leq 0.5$ at $2R/H = 0.37$, to $0.5 \leq Ca_{cr} \leq 0.6$ at $2R/H = 0.5$ and finally to $0.55 \leq Ca_{cr} \leq 0.625$ at $2R/H = 0.625$, suggesting that Ca_{cr} increases with increasing confinement. Contrary to the low viscosity ratio case, Ca_{cr} decreases with increasing confinement for the high viscosity ratio, i.e. $\lambda = 5$. Specifically, the critical capillary number decreases from $0.5 \leq Ca_{cr} \leq 0.6$ to $0.3 \leq Ca_{cr} \leq 0.35$ when one increases the confinement ratio from 0.55 to 0.8. Fig. 9 shows the snapshots of the droplet breakup process for $Ca = 0.35$, $\lambda = 5$ and $2R/H = 0.8$. The droplet deforms continuously and eventually breaks up into two equal-sized daughter droplets, as opposed to the unbounded case where the high viscosity ratio droplet ($\lambda > 4$) does not break regardless of the capillary number. Also, it is interestingly observed in Fig. 8 that the confinement ratio has small effect on the critical capillary number for $\lambda = 1$, which is

around 0.4. These findings agree well with the previous experimental and numerical studies [3,24]. However, in these reported works [3,24] through a large number of experiments and/or simulations, it was found that for $\lambda = 1$ that the critical capillary number first decreases and then increases with the confinement ratio. The minimum critical capillary number occurs at $2R/H = 0.5$. To capture this subtle variation of the critical capillary number with the confinement ratio, a large number of simulations are required which will be studied separately by exploiting massively parallel computing.

Even though the overall agreement is quite satisfactory between the present results and those obtained by Janssen et al. [3], some quantitative differences are also noticed. For example, Janssen et al. [3] experimentally found that binary breakup is expected to occur for a droplet with $\lambda = 1.0$ at $Ca = 0.45$ and $0.37 \leq 2R/H \leq 0.45$, whereas in our simulations ternary breakup is observed. Fig. 10 shows the snapshots of the droplet breakup process for $Ca = 0.45$, $\lambda = 1$ and $2R/H = 0.45$. As the droplet is stretched by the external shear flow, it first deforms to an ellipsoidal shape ($\dot{\gamma}t = 4$). The major axis lengthens while the minor axis shrinks, leading to the formation of a waist near the centre of droplet at $\dot{\gamma}t = 16$. The droplet is then elongated to a 'dumbbell' shape, and at the same time the bulbs at the end of droplet achieve a stable shape ($\dot{\gamma}t = 20$). At $\dot{\gamma}t = 25$, two visible necks are formed between the central portion of the droplet and bulbs. The droplet continues to thin and eventually breaks up into three parts (i.e., ternary breakup) with two daughter droplets having much larger size ($\dot{\gamma}t = 27$).

In addition, the previous experimental study indicated that the lowest Ca_{cr} for all of viscosity ratios ($0.3 \leq \lambda \leq 5$) and confinement ratios ($0.1 \leq 2R/H \leq 0.9$) is around 0.4 [3], but in our simulations the lowest Ca_{cr} is found between 0.3 and 0.35, which can be clearly seen in Fig. 8 for the case of $\lambda = 5$ and $2R/H = 0.8$. The reason for these differences remains unclear, and is likely to be the result of a combination of factors, including the experimental errors and model accuracy in describing the interfacial dynamics.

4. Conclusions

The influence of capillary number, viscosity ratio and confinement ratio have been systematically studied for droplet deformation and breakup in a simple shear flow. Increasing confinement leads to an increase in droplet deformation for a wide range of viscosity ratios, and the droplet with the same viscosity as the carrier fluid presents the largest deformation at all confinement ratios. The orientation angle of the deformed droplet decreases with increasing viscosity ratio. It is observed that the presence of walls has a more significant impact on both droplet deformation and orientation angle when the confinement ratio increases to 0.4 or higher. The flowfield inside and around the droplet shows that confinement and viscosity ratios can lead to a perplex pattern which may affect droplet behaviour. Finally, the critical capillary number, above which the droplet breakup occurs, is investigated for a broad range of flow conditions. Depending on the value of viscosity ratio, the confinement ratio has different effects on the critical capillary number: as the confinement increases, the critical capillary number increases for $\lambda < 1$ but decreases for $\lambda > 1$; and for $\lambda = 1$ the critical capillary number is kept at a value of around 0.4, regardless of the confinement ratio.

References

[1] G.I. Taylor, The formation of emulsions in definable fields of flow, J. Colloid Interface Sci. 38 (1934) 501–523.

[2] F.A. Morrison, Understanding Rheology, Oxford University Press, 2001.

[3] P.J.A. Janssen, A. Vananroye, P.V. Puyvelde, P. Moldenaers, P.D. Anderson, Generalized behavior of the breakup of viscous drops in confinements, J. Rheol. 54 (5) (2010) 1047–1060, URL: http://scitation.aip.org/content/sor/journal/jor2/54/5/10.1122/1.3473924.

[4] M.R. Kennedy, C. Pozrikidis, R. Skalak, Motion and deformation of liquid drops, and the rheology of dilute emulsions in simple shear flow, Comput. Fluids 23 (2) (1994) 251–278, URL: http://www.sciencedirect.com/science/article/pii/004579309490040X.

[5] S. Guido, M. Villone, Three-dimensional shape of a drop under simple shear flow, J. Rheol. 42 (1998) 395–415, URL: http://scitation.aip.org/content/sor/journal/jor2/42/2/10.1122/1.550942.

[6] A. Vananroye, P. Van Puyvelde, P. Moldenaers, Effect of confinement on the steady-state behavior of single droplets during shear flow, J. Rheol. 51 (1) (2007) 139–153, http://dx.doi.org/10.1122/1.2399089, URL: http://scitation.aip.org/content/sor/journal/jor2/51/1/10.1122/1.2399089.

[7] V. Cristini, Y.-C. Tan, Theory and numerical simulation of droplet dynamics in complex flows – a review, Lab Chip 4 (2004) 257–264, URL: http://pubs.rsc.org/en/content/articlehtml/2004/lc/b403226h.

[8] S. Guido, F. Greco, Dynamics of a liquid drop in a flowing immiscible liquid, Rheol. Rev. (2004) 99–142, URL: http://www.bsr.org.uk/rheology-reviews/RheologyReviews/liquid-drop-immiscible-liquid-GuidoGreco.pdf.

[9] P.V. Puyvelde, A. Vananroye, R. Cardinaels, P. Moldenaers, Review on morphology development of immiscible blends in confined shear flow, Polymer 49 (25) (2008) 5363–5372, http://dx.doi.org/10.1016/j.polymer.2008.08.055, URL: http://www.sciencedirect.com/science/article/pii/S0032386108007544.

[10] M. Minale, Models for the deformation of a single ellipsoidal drop: a review, Rheol. Acta 49 (8) (2010) 789–806, http://dx.doi.org/10.1007/s00397-010-0442-0.

[11] C.E. Chaffey, H. Brenner, A second-order theory for shear deformation of drops, J. Colloid Interface Sci. 24 (2) (1967) 258–269, http://dx.doi.org/10.1016/0021-9797(67)90229-9, URL: http://www.sciencedirect.com/science/article/pii/0021979767902299.

[12] J.M. Rallison, Note on the time-dependent deformation of a viscous drop which is almost spherical, J. Fluid Mech. 98 (1980) 625–633, http://dx.doi.org/10.1017/S0022112080000316, URL: http://journals.cambridge.org/article_S0022112080000316.

[13] J.M. Rallison, A numerical study of the deformation and burst of a viscous drop in general shear flows, J. Fluid Mech. 109 (1981) 465–482, URL: http://journals.cambridge.org/download.php?file=%2FFLM%2FFLM109%2FS002211208100116Xa.pdf&code=afc88fbdcd8cfaf45e74d9e8bd98cb77.

[14] F. Greco, Second-order theory for the deformation of a Newtonian drop in a stationary flow field, Phys. Fluids 14 (3) (2002) 946–954, http://dx.doi.org/10.1063/1.1445182, URL: http://scitation.aip.org/content/aip/journal/pof2/14/3/10.1063/1.1445182.

[15] S. Guido, Shear-induced droplet deformation: effects of confined geometry and viscoelasticity, Curr. Opin. Colloid Interface Sci. 16 (1) (2011) 61–70, http://dx.doi.org/10.1016/j.cocis.2010.12.001, URL: http://www.sciencedirect.com/science/article/pii/S1359029410001226.

[16] P. Maffettone, M. Minale, Equation of change for ellipsoidal drops in viscous flow, J. Non-Newtonian Fluid Mech. 78 (1998) 227–241, URL: http://ac.els-cdn.com/S0377025798000652/1-s2.0-S0377025798000652-main.pdf?_tid=dff6b528-f0e2-11e4-9bfa-00000aab0f6c&acdnat=1430581973_58d00b70d8ae847f6b0278389a56cf08.

[17] M. Minale, A phenomenological model for wall effects on the deformation of an ellipsoidal drop in viscous flow, Rheol. Acta 47 (2008) 667–675, URL: http:// download- v2. springer. com/ static/ pdf/ 111/ art%253A10. 1007%252Fs00397- 007- 0237- 0.pdf?token2=exp=1430583106 acl =%2Fstatic%2Fpdf%2F111%2Fart%25253A10. 1007%25252Fs00397- 007- 0237- 0.pdf* hmac=ff39c5831a50644cd93dd91a50ff042eefced0064b60370d315695fcd2cb594c.

[18] M. Shapira, S. Haber, Low Reynolds number motion of a droplet in shear flow including wall effects, Int. J. Multiphase Flow 16 (2) (1990) 305–321, URL: http://www.sciencedirect.com/science/article/pii/030193229090061M.

[19] V. Sibillo, G. Pasquariello, M. Simeone, V. Cristini, S. Guido, Drop deformation in microconfined shear flow, Phys. Rev. Lett. 97 (5) (2006) 1–4, http://dx.doi.org/10.1103/PhysRevLett.97.054502, 054502.

[20] J. Li, Y.Y. Renardy, M. Renardy, Numerical simulation of breakup of a viscous drop in simple shear flow through a volume-of-fluid method, Phys. Fluids 12 (2) (2000) 269–282, URL: https://www.math.vt.edu/people/renardyy/Research/Publications/feb2000.pdf.

[21] Y.Y. Renardy, V. Cristini, Effect of inertia on drop breakup under shear, Phys. Fluids 13 (1) (2001) 7–13, http://dx.doi.org/10.1063/1.1331321.

[22] Y. Renardy, The effects of confinement and inertia on the production of droplets, Rheol. Acta 46 (4) (2007) 521–529, http://dx.doi.org/10.1007/s00397-006-0150-y.

[23] P.J.A. Janssen, P.D. Anderson, Boundary-integral method for drop deformation between parallel plates, Phys. Fluids 19 (2007) 1–11, 043602, URL: http://www.mate.tue.nl/mate/pdfs/7660.pdf.

[24] A. Vananroye, P.J.A. Janssen, P.D. Anderson, P. Van Puyvelde, P. Moldenaers, Microconfined equiviscous droplet deformation: comparison of experimental and numerical results, Phys. Fluids 20 (2008) 1–10, http://dx.doi.org/10.1063/1.2835312, 013101, URL: http://scitation.aip.org/content/aip/journal/pof2/20/1/10.1063/1.2835312.

[25] V. Cristini, J. Blawzdziewics, M. Loewenberg, An adaptive mesh algorithm for evolving surfaces: simulations in drop breakup and coalescence, J. Comput. Phys. 168 (2001) 445–463, URL: http://www.sciencedirect.com/science/article/pii/S0021999101967130.

[26] O. Shardt, J. Derksen, S.K. Mitra, Simulations of droplet coalescence in simple shear flow, Langmuir 29 (21) (2013) 6201–6212, http://dx.doi.org/10.1021/la304919p.

[27] A.K. Gunstensen, D.H. Rothman, S. Zaleski, G. Zanetti, Lattice Boltzmann model of immiscible fluids, Phys. Rev. A 43 (1991) 4320–4327, http://dx.doi.org/10.1103/PhysRevA.43.4320.

[28] M.R. Swift, W.R. Osborn, J.M. Yeomans, Lattice Boltzmann simulation of nonideal fluids, Phys. Rev. Lett. 75 (1995) 830–833, http://dx.doi.org/10.1103/PhysRevLett.75.830.

[29] X. Shan, H. Chen, Lattice Boltzmann model for simulating flows with multiple phases and components, Phys. Rev. E 47 (1993) 1815–1819, http://dx.doi.org/10.1103/PhysRevE.47.1815.

[30] X. He, S. Chen, R. Zhang, A lattice Boltzmann scheme for incompressible multiphase flow and its application in simulation of Rayleigh–Taylor instability, J. Comput. Phys. 152 (2) (1999) 642–663, http://dx.doi.org/10.1006/jcph.1999.6257, URL: http://www.sciencedirect.com/science/article/pii/S0021999199962575.

[31] H. Xi, C. Duncan, Lattice Boltzmann simulations of three-dimensional single droplet deformation and breakup under simple shear flow, Phys. Rev. E 59 (1999) 3022–3026, http://dx.doi.org/10.1103/PhysRevE.59.3022.

[32] R. van der Sman, S. van der Graaf, Emulsion droplet deformation and breakup with lattice Boltzmann model, Comput. Phys. Commun. 178 (7) (2008) 492–504, http://dx.doi.org/10.1016/j.cpc.2007.11.009, URL: http://www.sciencedirect.com/science/article/pii/S0010465507004675.

[33] H. Liu, A.J. Valocchi, Three-dimensional lattice Boltzmann model for immiscible two-phase flow simulations, Phys. Rev. E 85 (2012) 1–14, http://dx.doi.org/10.1103/PhysRevE.85.046309, 046309.

[34] S. Farokhirad, T. Lee, J.F. Morris, Effects of inertia and viscosity on single droplet deformation in confined shear flow, Commun. Comput. Phys. 13 (3) (2013) 706–724, URL: http://www.academia.edu/8043985/Effects_of_Inertia_and_Viscosity_on_Single_Droplet_Deformation_in_Confined_Shear_Flow.

[35] A. Komrakova, O. Shardt, D. Eskin, J.J. Derksen, Lattice Boltzmann simulations of drop deformation and breakup in shear flow, Int. J. Multiphase Flow 59 (2014) 24–43, URL: http://www.sciencedirect.com/science/article/pii/S0301932213001547.

[36] A. Gupta, M. Sbragaglia, Deformation and breakup of viscoelastic droplets in confined shear flow, Phys. Rev. E 90 (2014) 1–14, http://dx.doi.org/10.1103/PhysRevE.90.023305, 023305.

[37] H. Liu, Y. Ju, G. Xi, Y. Zhang, Lattice Boltzmann modeling of contact angle and its hysteresis in two-phase flow with large viscosity difference, Phys. Rev. E 92 (2015).

[38] H. Liu, Y. Zhang, A.J. Valocchi, Lattice Boltzmann simulation of immiscible fluid displacement in porous media: homogeneous versus heterogeneous pore network, Phys. Fluids 27 (2015), http://dx.doi.org/10.1063/1.4921611.

[39] J. Brackbill, D. Kothe, C. Zemach, A continuum method for modeling surface tension, J. Comput. Phys. 100 (1992) 335–354, URL: http://ac.els-cdn.com/002199919290240Y/1-s2.0-002199919290240Y-main.pdf?_tid=c67f7a46-f0e0-11e4-9008-00000aab0f27&acdnat=1430581072_91f0c5465fa22f45755df6ed0232b289.

[40] I. Halliday, A.P. Hollis, C.M. Care, Lattice Boltzmann algorithm for continuum multicomponent flow, Phys. Rev. E 76 (2007) 1–13, http://dx.doi.org/10.1103/PhysRevE.76.026708, 026708.

[41] H. Liu, Y. Zhang, A.J. Valocchi, Modeling and simulation of thermocapillary flows using lattice Boltzmann method, J. Comput. Phys. (2012) 4433–4453, URL: http://www.sciencedirect.com/science/article/pii/S0021999112000940.

[42] Z. Guo, C. Zheng, B. Shi, Discrete lattice effects on the forcing term in the lattice Boltzmann method, Phys. Rev. E 65 (2001) 1–6, http://dx.doi.org/10.1103/PhysRevE.65.046308, 046308.

[43] Y.Q. Zu, S. He, Phase-field-based lattice Boltzmann model for incompressible binary fluid systems with density and viscosity contrasts, Phys. Rev. E 87 (2013) 1–23, http://dx.doi.org/10.1103/PhysRevE.87.043301, 043301.

[44] H. Liu, Y. Zhang, Phase-field modeling droplet dynamics with soluble surfactants, J. Comput. Phys. 229 (24) (2010) 9166–9187, http://dx.doi.org/10.1016/j.jcp.2010.08.031, URL: http://www.sciencedirect.com/science/article/pii/S002199911000478X.

[45] M. Latva-Kokko, D.H. Rothman, Diffusion properties of gradient-based lattice Boltzmann models of immiscible fluids, Phys. Rev. E 71 (2005) 1–8, http://dx.doi.org/10.1103/PhysRevE.71.056702, 056702.

[46] H. Liu, Y. Zhang, Droplet formation in microfluidic cross-junctions, Phys. Fluids 23 (2011) 1–12, http://dx.doi.org/10.1063/1.3615643, 082101.

[47] T. Zhang, B. Shi, Z. Guo, Z. Chai, J. Lu, General bounce-back scheme for concentration boundary condition in the lattice-Boltzmann method, Phys. Rev. E 85 (2012) 1–14, http://dx.doi.org/10.1103/PhysRevE.85.016701, 016701.

[48] S. Kwak, C. Pozrikidis, Adaptive triangulation of evolving, closed, or open surfaces by the advancing-front method, J. Comput. Phys. 145 (1) (1998) 61–88, http://dx.doi.org/10.1006/jcph.1998.6030, URL: http://www.sciencedirect.com/science/article/pii/S0021999198960302.

Haihu Liu is an Associate Professor at Xi'an Jiaotong University, China. He received his BEng and MEng degrees in Fluid Machinery and Engineering from Xi'an Jiaotong University in 2004 and 2007, respectively. He then joined the James Weir Fluids Laboratory as a PhD student in 2007. After awarded his PhD in 2011, he worked as a post-doctoral research associate in the Department of Civil & Environmental Engineering in the University of Illinois at Urbana-Champaign, USA. In September 2013, he joined University of Strathclyde as a Lecturer and then became an Associate Professor at Xi'an Jiaotong University China in 2014.

Nikolaos Ioannou obtained a 5-year Diploma, equivalent to Master of Science degree, in Mechanical engineering from the School of Mechanical Engineering, National University of Athens in 2010. In 2014, he obtained a Master in Computational Mechanics from the same institution. He is a Ph.D candidate under the supervision of Prof. Yong-hao Zhang in the Mechanical and Aerospace department of the University of Strathclyde, and a member of the James Weir Fluids Laboratory since December 2012. His research involves interfacial dynamics at the microscale and non-Newtonian fluids.

Yonghao Zhang is Weir Professor of Thermodynamics and Fluid Mechanics at University of Strathclyde, UK. He leads the James Weir Fluids Laboratory (http://www.jwfl.org.uk) to advance our understanding of fundamental flow physics and chemistry in micro/nano systems, with the aim of utilising these research advances to develop new technologies with capabilities beyond any currently conceived. After his PhD study in Mechanical Engineering at University of Aberdeen, UK, in 2001, he worked as a Scientist, then Senior Scientist at STFC Daresbury Laboratory, UK. In 2007, He joined University of Strathclyde as John Anderson Research Lecturer.